ACS Catalysis

Research Article

Cite This: ACS Catal. 2020, 10, 1428−1438

pubs.acs.org/acscatalysis

Structure Sensitivity in Steam and Dry Methane Reforming over Nickel: Activity and Carbon Formation

Charlotte Vogt, Jelle Kranenborg, Matteo Monai, and Bert M. Weckhuysen*

Inorganic Chemistry and Catalysis Group, Debye Institute for Nanomaterials Science, Utrecht University, Universiteitsweg 99, 3584 CG Utrecht, The Netherlands

Supporting Information

ABSTRACT: Hydrogen is currently mainly produced via steam reforming of methane (SMR: $CH_4 + H_2O \rightarrow CO + 3H_2$). An alternative to this process, utilizing carbon dioxide and thus potentially mitigating its environmentally harmful emissions, is dry methane reforming (DMR: $CH_4 + CO_2 \rightarrow 2CO + 2H_2$). Both of these reactions are structure sensitive, that is, not all atoms in a catalytic metal nanoparticle have the same activity. Mapping this structure sensitivity and understanding its mechanistic workings provides ways to design better, more efficient, and more stable catalysts. Here, we study a range of SiO_2-supported Ni nanoparticles with varying particle sizes (1.2−6.0 nm) by operando infrared spectroscopy to determine the active mechanism over Ni (carbide mechanism) and its kinetic dependence on Ni particle size. We establish that Ni particle sizes below 2.5 nm lead to a different structure sensitivity than is expected from and implied in literature. Because of the identification of CH_xD_x species with isotopically labeled experiments, we show that CH_4 activation is not the only rate-limiting step in SMR and DMR. The recombination of C and O or the activation of CO is likely also an important kinetically limiting factor in the production of synthesis gas in DMR, whereas for SMR the desorption of the formed CO becomes more kinetically limiting. Furthermore, we establish the Ni particle size dependence of carbon whisker formation. The optimal Ni particle size both in terms of activity for SMR and DMR, at 500 and 600 °C, and 5 bar, was found to be approximately 2−3 nm, whereas carbon whisker formation was found to maximally occur at approximately 4.5 nm for SMR and for DMR increased with increasing particle size. These results have direct practical applications for tuning of activity and selectivity of these reactions, while providing fundamental understanding of their working.

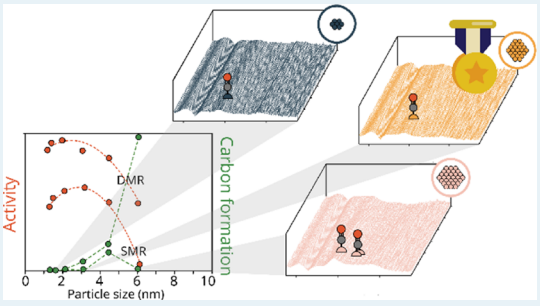

KEYWORDS: *steam methane reforming, dry methane reforming, nickel, structure sensitivity, spectroscopy, Fourier transform infrared spectroscopy, nickel*

INTRODUCTION

Most hydrogen that is industrially produced today is done so via a heterogeneous catalytic process called steam methane reforming (SMR, eq 1) where water and methane react to form synthesis gas, a mixture of CO an H_2.[1−3] In a post-crude oil-based society, hydrogen may become an important energy carrier, and a wide variety of fuels and chemicals can be produced from synthesis gas,[2−5] for example, by such industrially relevant processes like the Fischer−Tropsch synthesis of hydrocarbons.[6−8] Although technically synthesis gas can be produced from waste (i.e., biomass and municipal waste), it is currently still mainly produced from coal and natural gas, which, depending on the source, makes crude oil alternative processes such as Fischer−Tropsch synthesis, less sustainable than advertised.[5] From an environmental standpoint, it would be much more interesting to utilize greenhouse gas CO_2 as feedstock for methane reforming to aid in the mitigation of its release into the atmosphere.[9] This, if the processes can be fully optimized, may bring down the overall environmental footprint of the production of synthesis gas and therefore also all subsequent fuels and chemicals produced from it.[10] Dry methane reforming (DMR, eq 2), that is, the reaction which produces synthesis gas from methane and carbon dioxide, has thus been gaining recent experimental interest.[11] The enthalpies of formation of some relevant reactions involving methane are given in eqs 1−5.[1,12−14]

$$CH_4 + H_2O \rightarrow CO + 3H_2 \qquad \Delta H_{298\,K} = +206\ \text{kJ/mol} \tag{1}$$

$$CH_4 + CO_2 \rightarrow 2CO + 2H_2 \qquad \Delta H_{298\,K} = +247\ \text{kJ/mol} \tag{2}$$

$$CH_4 + 1/2O_2 \rightarrow CO + 2H_2 \qquad \Delta H_{298\,K} = -36\ \text{kJ/mol} \tag{3}$$

$$CH_4 + 2O_2 \rightarrow CO_2 + 2H_2O \qquad \Delta H_{298\,K} = -803\ \text{kJ/mol} \tag{4}$$

$$CH_4 \rightarrow C + 2H_2 \qquad \Delta H_{298\,K} = 75\ \text{kJ/mol} \tag{5}$$

Received: September 28, 2019
Revised: December 18, 2019
Published: December 18, 2019

DOI: 10.1021/acscatal.9b04193
ACS Catal. 2020, 10, 1428−1438

Both DMR and SMR are endothermic (eqs 1 and 2, and Figure S1). In the case of SMR, high H_2O/CH_4 ratios are needed to limit, for example, coke formation at reaction temperatures higher than 700 °C.[1,12−14] Another (intermediate) reaction that can occur is the addition of oxygen to methane, which is called the partial oxidation of methane (POM, eq 3), an exothermic reaction that yields a lower ratio of H_2/CO.[12,14,15] POM is in direct competition with the complete combustion of methane (eq 4), which is highly exothermic and leads to the release of CO_2. An often-unwanted side-reaction to methane reforming reactions is the production of C (eq 5), which may deactivate the catalyst. The water−gas shift reaction, where CO and H_2O react to form CO_2 and H_2, is an exothermic reaction that connects SMR and DMR, and it affects the H_2/CO ratio that can be thermodynamically obtained in the presence of H_2O and CO_2 (see Figure S2). This phenomenon is leveraged on industrial scale to tune the final gas composition.[2,3]

Each of the above chemical reactions can be catalyzed by supported nickel catalysts. Although nickel is a good catalyst for both SMR and DMR, it requires relatively high reaction temperatures (600−900 °C) to obtain high syngas yields;[16−20] yet under these conditions the catalyst is prone to coking[9,19,21,22] and deactivation by metal sintering.[14,23] Hence, it is quite a challenge to steer the selectivity of the reactions to syngas (CO) and to achieve high enough yields at reasonable operation temperatures (to increase the stability of the catalyst), as the reactions (eq 1 and eq 2) are highly endothermic.

Many steps in the mentioned reactions are what is termed structure sensitive.[24−27] Structure sensitive reactions involve rate-determining steps where not all active sites of the exposed surface of a supported metal catalyst nanoparticle have the same intrinsic activity. By changing the size of a metal nanoparticle, one changes the fraction of available active surface sites.[28] Small metal nanoparticles will have relatively more stepped or edge sites than a larger metal nanoparticle, which will have a larger ratio of flat or terrace sites. In the case of SMR and DMR, catalyst activity, selectivity, and stability (i.e., metal sintering as well as deactivation by carbon deposition) can be affected by the particle sizes of the supported catalysts. The activation of methane, the recombination of C and O, and C−C coupling to form carbon nanofibers may all be structure sensitive aspects for both reactions.[29−33] Although it is important to realize that industrial reactors are operated at thermodynamic equilibrium, we should consider that the extent to which the thermodynamic equilibrium including carbon deposition may be reached may vary with varying mean nanoparticle size. Thus, it is interesting to study the structure sensitivity of both reactions as concepts to steer the activity, selectivity, and even stability of these reactions.

Figure 1a,b displays a schematic overview of the two possible reaction pathways CH_4 can follow to the main reaction products CO and CO_2 in the SMR and DMR reactions.[18,32,34,35] In this way, two pathways can be generalized, which are (i) a route in which CH_x intermediates are oxidized and (ii) a route in which methane is first fully stripped of its H-atoms and subsequently a carbon adatom is oxidized. In reality, on any given catalyst, both pathways likely occur but different steps may be significantly faster than the others depending on, amongst others, the mean particle size and reaction conditions. This could be a potential reason why disagreement exists in literature as to which of the reaction intermediates of these pathways are kinetically relevant.[32,34,36] The subtlety here lies in the fact that different sites have higher activity to C−H activation than to C═O recombination.[26] C−H-activation (σ-bond) preferentially occurs on highly under-coordinated sites, preferably single metal atoms, whereas the activation and cleavage of π-bonds occurs preferentially over "defect" sites like B_5 sites where an incoming adatom incurs five metal atoms.[24,25,37−40]

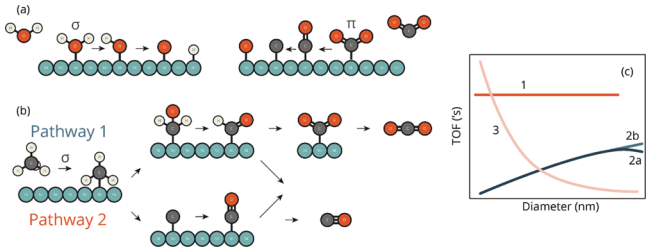

Figure 1. (a) Cleavage of σ-bonds is necessary for the activation of H_2O and CH_4, whereas the activation of CO_2 requires the cleavage of π-bonds. (b) Schematic representation of the possible reaction pathways for both SMR and DMR. Two pathways can be generalized, a formyl-intermediate route (pathway 1), and a direct carbide route (pathway 2). (c) TOF classes as commonly portrayed (adapted from van Santen[26]), with class 1 structure insensitivity, class 2 π-bond structure sensitivity, and class 3 σ-bond structure sensitivity.

The different relative abundance of the abovementioned active sites on metal nanoparticles of different sizes gives rise to the generally accepted classes of structure sensitivity, as plotted in Figure 1c.[25,26] For structure insensitive reactions, the turnover frequency (TOF) does not change with particle size (class 1 in Figure 1c). For the activation of a π-bond, for example, in C═O, the class of structure sensitivity is 2. Here, the TOF increases with increasing particle size as a certain degree of site coordination is required for the activation of such chemical bonds, and it may subsequently decrease (class 2a) or stay constant (class 2b). This subdivision between 2a and 2b is under debate, but arguably experimentally observed for, for example, CO_2 hydrogenation[41] versus the Fischer−Tropsch synthesis of hydrocarbons.[42] If the rate-determining step involves the activation of a σ-bond such as in a C−H bond, the class of structure sensitivity is normally denoted as class 3 in Figure 1c. For this class, the TOF generally increases with decreasing metal nanoparticle size as these chemical bonds are preferentially cleaved over highly under-coordinated atoms in the metal nanoparticle.

Therefore, on a catalyst where C−H activation is difficult, pathway 1 (Figure 1b) might be much more prevalent, whereas on a catalyst where the recombination of a C and O adatom is very slow relative to the activation of C−H bonds, pathway 2 may be prevalent. This may lead to different kinetics, product distribution and catalyst stability over catalysts having different Ni nanoparticle sizes. Furthermore, if the recombination of C and O is relatively slow, one might expect the formation of additional carbon deposits to be a possibility. Indeed, carbon nanofibers grow in what is regarded as a deactivation mechanism in SMR and DMR. This is an interesting phenomenon as in a post-crude oil-based society, it can be of interest to make C materials from CH_4,[43] making use of eq 5.

It is thus interesting to systematically study the structure sensitivity of the SMR and DMR reactions and to identify

DOI: 10.1021/acscatal.9b04193
ACS Catal. 2020, 10, 1428−1438

relevant experimental descriptors linked to the activity, selectivity, and stability of these reactions with the intention to increase mechanistic understanding and provide new insights for advanced materials design. More specifically, we will study the effect of structure sensitivity not only on the activity of SMR and DMR but also on the carbon nanofiber growth, which is a side reaction of SMR and DMR, leading to catalyst deactivation (yet is conceptually interesting for C material production from methane). Thus, we set out to study with a set of well-defined SiO_2-supported Ni catalysts with metal nanoparticles in the range of 1.2−6 nm (see Tables 1 and S3 for an overview of the materials used). Operando infrared (IR) spectroscopy was used to find experimental descriptors for activity in combination with transmission electron microscopy (TEM) and thermogravimetric analysis (TGA) to study carbon nanofiber growth. It was found that a maximum growth rate in carbon nanofibers was found for supported Ni metal particles of approximately 4.5 nm for SMR, and of increasing mean Ni particle size for DMR, whereas the optimal particle size in terms of (short term) stability and activity toward the desired products in both SMR and DMR is ∼3 nm.

Table 1. Overview of the Ni/SiO_2 Catalyst Materials Studied in This Work, Including Their Metal Nanoparticle Size after Reduction as Determined by High-Angle Annular Dark-Field Scanning Transmission Microscopy, and the Weight Loading of Each Catalyst Sample

catalyst code	particle size from HAADF−STEM (nm)[a]	weight loading Ni (%)
1	1.2 ± 0.5	4.7
2	1.4 ± 0.4	5.0
3	2.0 ± 0.8	6.7
4	3.1 ± 0.9	11.8
5	4.4 ± 2.4	19.5
6	6.0 ± 1.9	60.0

[a]Particle size distributions determined after the reduction step (and reoxidation by exposure to air) of at least 120 nanoparticles, see Vogt et al.[41] for additional details on HAADF−STEM analysis.

METHODS AND MATERIALS

Catalyst Materials and Related Characterization. Ni/SiO_2 catalyst materials were prepared via homogeneous deposition precipitation and coprecipitation according to, for example, Ermakova and Ermakov.[44] Although pure SiO_2 support is not generally used in industrial settings, it is an excellent support to minimize support effects as SiO_2 is the only relevant support with minimal metal−support interaction or influence of Lewis acidity. Hence, to separate the particle size effect from any other influences, this support was used. The reported activity of the catalysts in this study proves the relevance of this system. The catalyst samples under investigation have varying Ni mean particle sizes, synthesized by variation of the metal salt concentration during preparation.[41] Table 1 provides an overview of the weight loading and mean particle size of the different catalyst materials under study. Temperature-programmed reduction with hydrogen (Linde 6.0) was performed in a Tristar II series analyzer and is reported elsewhere.[41] The thus determined reduction profiles were a 5 °C min^{-1} ramp to 550 °C, held for 1 h. Fresh, reduced and passivated, and spent samples (of different reaction times) were examined with TEM in a FEI Tecnai12 operated at 120 kV or in a FEI Tecnai20F operated at 200 kV. The catalyst samples were crushed and suspended in ethanol under ultrasonic vibration. A drop of this suspension was deposited on a holey carbon film on a 300-mesh copper grid. The measured NiO metal particle sizes, listed in Table 1, under HAADF−STEM are average values (>100 Ni metal nanoparticles). We refer to the Supporting Information (see also Figures S3 and S4) for more details. The catalysts were analyzed by (S)TEM as fresh, reduced, and spent samples. Additional characterization data can be found elsewhere.[41] TGA coupled with mass spectrometry (MS) of all spent samples was performed by use of a PerkinElmer Pyris1TGA instrument, see Section "Carbon formation" of the Supporting Information for more details.

FT-IR Spectroscopy. Operando Fourier-transform infrared (FT-IR) spectroscopy measurements were performed to study reactants, reaction intermediates, and reaction products in SMR and DMR over SiO_2-supported Ni catalysts. Figure S5 shows the setup used to measure time-resolved operando FT-IR spectra to study the effect of different mean particle sizes on reaction intermediates and catalyst activity at different temperatures. These measurements were carried out using a Bruker Tensor 37 FT-IR spectrometer with a DTGS detector. Spectra were recorded every 26.5 s for each experiment. On-line product analysis was performed with an Interscience custom-built Global Analyzer Solutions (G.A.S.) Compact $GC_{4.0}$ gas chromatograph (GC) with a time resolution of around 10 s for lower hydrocarbons. Small amounts of ethane are also formed and more details on the catalyst activity and selectivity can be found in the Supporting Information.

The catalytic experiments were carried out in a Specac High-Temperature transmission IR reaction cell. To this end, the catalyst powders were pressed into wafers of approximately 16 mm in diameter, and around 0.1 mm thickness weighing between 10 and 15 mg. These self-supported catalyst wafers were created using a Specac Laboratory Pellet Press, a diaphragm vacuum pump, and around 4 t of pressure. After the previously mentioned in situ reduction procedure, the temperature of the reaction cell was brought to 500 °C with a 5 °C min^{-1} ramp, and the feed was flushed through a bypass in the setup for 20 min for the feedstock content to stabilize. The reactants were introduced through Bronkhorst EL-FLOW Mass Flow Controllers. CH_4 was fed at 9.1 mL min^{-1} for both SMR and DMR. For SMR, He was flown at 33.5 mL min^{-1} through a stainless-steel saturator containing Milli-Q water, to provide 2.1 mL min^{-1} water. The Supporting Information lists details on flows, GHSV, and WHSV used for each of the catalytic experiments. All following feed gasses are Linde, CH_4 4.5, He 5.0, H_2 6.0, and CO_2 4.0 purity. Isotopically labeled experiments were performed with carbon-13 labeled methane (99 atom %, Sigma-Aldrich) or D_2O (99.9 atom %, Sigma-Aldrich). After flushing, the reactor temperature was held for 1 h at 500 °C, then the cell was heated to 600 °C at a ramp rate of 5 °C min^{-1} and kept there for 1 h. The application of operando FT-IR spectroscopy with on-line GC product analysis in one setup serves to relate catalytic activity to the presence of different gaseous products and adsorbed reaction intermediates.

RESULTS AND DISCUSSION

Catalytic Activity Measurements. A set of six well-characterized and defined[41] SiO_2-supported Ni nanoparticles

DOI: 10.1021/acscatal.9b04193
ACS Catal. 2020, 10, 1428−1438

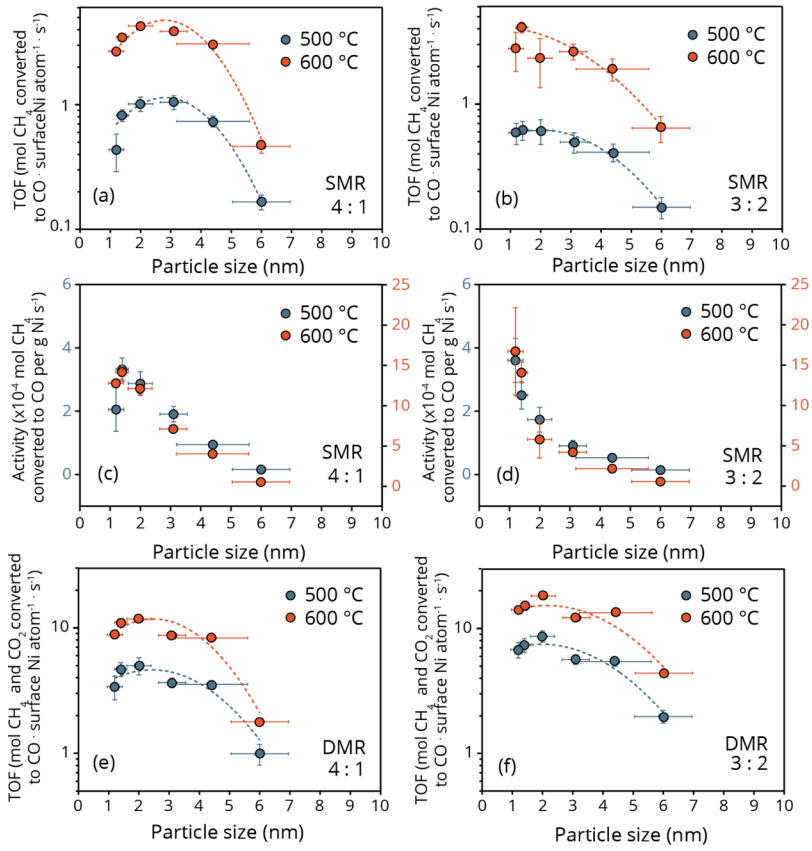

Figure 2. (a,b,e,f) TOF plotted against Ni metal nanoparticle size for SMR and DMR at different feedstock ratios of $CH_4/H_2O/CO_2$ at 500 and 600 °C and 5 bar. A second-order polynomial fit is drawn through the TOF points as an eye guide. (c,d) Activity per gram of Ni for SMR. Additional activity trends can be found in the Supporting Information.

with a Ni metal nanoparticle size varying between 1.2 and 6 nm (see Tables 1, and S3) were tested for SMR and DMR. This was done in an operando FT-IR spectroscopy setup and by using different feedstock ratios to gain insight into the rate-determining step at different partial pressures of the different reaction intermediates. Turnover frequencies (TOFs) and activity per gram of Ni, as measured in the operando FT-IR spectroscopy setup, have been determined for the SMR reaction at 500 and 600 °C, 5 bar pressure, for a 4:1 CH_4/H_2O ratio and a 3:2 ratio, and for the DMR reaction for CH_4/CO_2. Traditionally, a steam to carbon (S/C) ratio of 2.5 or above is usually chosen for Ni catalysts to avoid carbon formation.[45] However, high S/C ratios require more energy to produce excess steam, larger equipment and investment, and are thus both economically and energetically unfavorable. A drawback is that a low S/C ratio increases the methane slip-off from the reformer, but this can be addressed by increasing the reformer outlet temperature to about 900 °C.[46] Notably, noble metals such as Rh and Ru could be used because they are more resistant to carbon formation, but because of their high costs, research efforts are currently devoted to develop Ni catalysts showing resistance to carbon formation.[47] This can be achieved by catalyst design, for example, by changing the metal−support interactions,[48] and here we explore Ni nanoparticle size control as a valuable strategy. Hence, these ratios were chosen. The TOF was calculated based on the exposed metal surface area, as determined by the Ni mean particle sizes by HAADF−STEM after reduction, and these TOF numbers were then plotted against the Ni mean nanoparticle size for each of the catalyst materials after reduction. Spent particle size analysis was performed to determine whether the particles had significantly changed in size during reaction (see Supporting Information). Furthermore, the activity per gram of Ni was calculated. The result of this catalytic performance evaluation is shown in Figure 2. Additional activity data can be found in the Supporting Information (Figures S6−S14).

The trend in TOF plotted in Figure 2a−e for a large surplus of methane (4:1) is that there is a maximum in the surface-normalized activity at ∼2−3 nm. For the lower ratio of methane to reactant (3:2, Figure 2b,f), this trend becomes less apparent. In catalysis, the trend in TOF for a structure sensitive catalytic reaction is dependent on its rate-determining step (Figure 1c). Evidently in our results there is a shift in the dominant rate-determining step with a change in feedstock ratio. As explained in Figure 1, we may expect a difference in structure sensitivity classes when changing the oxidant to CO_2 (π-bond cleavage) from H_2O (σ-bond cleavage) if these steps were kinetically limiting. Yet as the trends are relatively similar for both SMR and DMR in Figure 2, it is likely that the activation of the oxidizing species (H_2O vs CO_2) is not a key kinetically limiting factor in SMR and DMR over Ni over the particle sizes studied in this work. Notably, thermodynamic calculations show that Ni oxidation to NiO is not favorable under any of the studied conditions. Whereas nanoparticles may have slightly different thermodynamics than bulk phases, we argue that deactivation by oxidation is not occurring even on the smallest nanoparticles, as the TOF observed for a 3:2 ratio of CH_4/H_2O is higher than for the more reducing feedstock ratio of 4:1.

DOI: 10.1021/acscatal.9b04193
ACS Catal. 2020, 10, 1428−1438

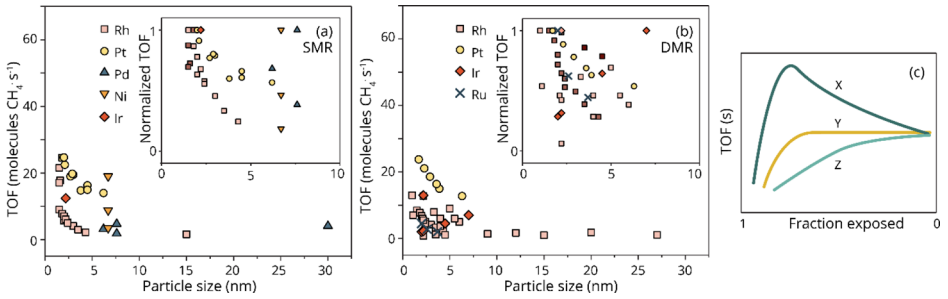

Figure 3. (a,b) TOF trends as reported in literature for (a) SMR and (b) DMR. The insets represent the TOF trends, normalized per literature work (i.e., the largest value in each study was set to 1). The symbols represent the metals, different literature works have different symbol fill color. (c) Schematic TOF trends as reported by Che and Bennett (Figure 25 of ref 25).

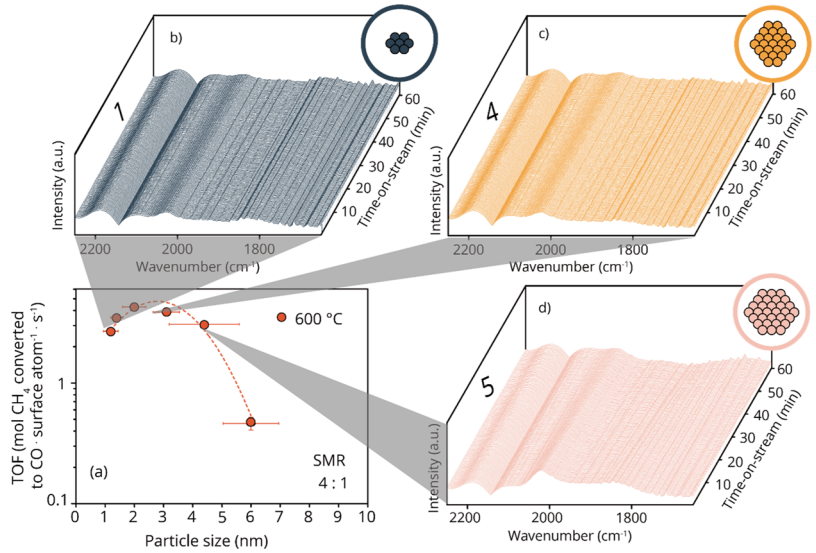

Figure 4. (a) TOF plot of SMR at 4:1 ratio of CH_4/H_2O, and (b−d) operando FT-IR spectra recorded simultaneously during the activity measurements.

Structure Sensitivity. Figures 3a,b gives an overview of the metal particle size-dependent TOF trends for both SMR (Figure 3a) and DMR (Figure 3b) reactions one can find in the open literature for, for example, Rh, Pt, Pd, In, Ru, or Ni. The Supporting Information gives an overview of the values used to compile Figures 3a,b as well as the related references. The inset in both Figures 3a,b shows the TOF values normalized for each study (i.e., the largest value in each study was set to 1) and thus shows particle size trends relative to each experimental setup. The metals are indicated by symbols, and color makes a distinction between two studies of the same metal. Figure S15 shows the same data as plotted in Figures 3a,b respectively, but plotted on a logarithmic scale. For a seemingly arbitrary reason, whereas most TOF values are generally plotted on a logarithmic scale, the TOF values for σ-bond activation are generally plotted on a linear scale. This accentuates what one could see as an exponential trend, but as trends for all other types of structure sensitivity are done so on a logarithmic scale, we plot both here for consistency and clarity. One can note in Figures 3a,b that there is a general increase in activity with decreasing particle size for most metals for SMR. For DMR, a slight decrease can be observed for very small nanoclusters. It is also interesting to note that it is commonplace for class 2 type structure sensitivity (e.g., Fischer Tropsch synthesis) to plot TOF trends on a logarithmic scale, which would significantly decrease the observed trends in the case of class 3 type structure sensitivity.

For noble metals such as Rh, it is relatively easy to create small nanoparticles, and the literature thus contains studies even down to 2 nm nanoclusters for both reactions. One can observe that for non-noble metal and more industrially relevant catalysts such as Ni, the information on particle size is incomplete particularly in the very small particle size regime. As mentioned, it has become common practice for class 3 type structure sensitivity (the activation of σ-bonds) to be drawn with the TOF as exponentially increasing toward smaller metal nanoparticle sizes (see Figure 1c).[26] In Figure 3c, we show an adaption of particle size effect classification from Che and Bennett (Figure 25 of their original paper).[25] Whereas "Figure 7" from the same paper by Che and Bennett is the figure that is often adapted with respect to structure sensitivity classification (as also done by us in Figure 1c), we believe Figure 3c to be more relevant to the discussion. We postulate that antipathetic behavior (decreasing activity with decreasing particle size) will exist for both structure sensitive and structure insensitive reactions when particle sizes (clusters) are small enough as both σ- and π-bonds are involved in a real catalytic reaction which is made up of several sequential elementary reaction steps. This discussion is relevant for SMR and DMR, and we propose the actual TOF trend should be drawn as line "X" in

DOI: 10.1021/acscatal.9b04193
ACS Catal. 2020, 10, 1428−1438

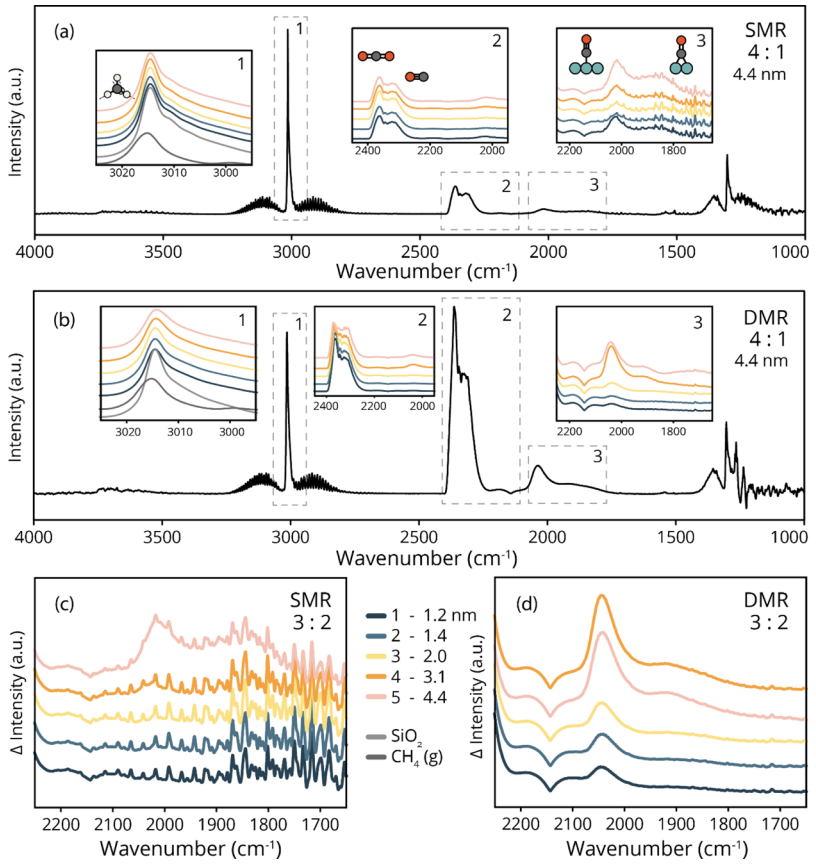

Figure 5. FT-IR spectra of the different SiO_2-supported Ni nanoparticles in (a) SMR and (b) DMR at 4:1 ratio of $CH_4/H_2O/CO_2$ at 500 °C and 5 bar. CO_{ads} stretching vibration region for (c) SMR and (d) DMR at 3:2 ratio of $CH_4/H_2O/CO_2$. The Supporting Information shows waterfall plots of all consecutive operando FT-IR spectra, of 3:2 and 4:1 ratios, and at 500 and 600 °C and 5 bar.

Figure 3c, with decreasing activity for very small nanoparticle sizes.

We can rationalize that for SMR and DMR, this decrease in TOF for decreasing particle sizes is also a logical trend to be observed, as a combination of sites is preferred for the different types of bonds that need to be cleaved, and the reaction involves both σ- and π-bonds. From these plots alone, we hence cannot yet say if the rate-determining step is the activation of a C−H bond, or the recombination of C═O, or, for example, its desorption. However, particularly in SMR, it seems that upon increasing the CH_4 ratio (Figure 2a vs 2b), the activation of CH_4 becomes a more important kinetic limitation as we here observe that smaller particles are more active.

Operando FT-IR Spectroscopy. To determine whether the observed TOF trends could be related to any of the surface reaction intermediates during the SMR and DMR reactions performed, operando FT-IR spectroscopy experiments were performed. The results of such experiments are summarized in Figure 4, where we obtain both the catalyst activity, selectivity, and yield and at the same time measure time-resolved operando spectroscopy data. FT-IR spectra are shown for a small, medium, and large Ni nanoparticle in Figures 4b−d, corresponding to the TOF plot in Figure 4a. Yet to distinguish differences in the spectra, they should be examined more closely. Figure 5a shows a full FT-IR spectrum from a typical SMR experiment, with different regions of interest marked as panels 1, 2, and 3. In this case, we show the results for SMR and DMR, at a temperature of 500 and 600 °C and 5 bar pressure. The complete list of operando FT-IR spectroscopy results are given in the Supporting Iinformation (Figures S16−S23). When assessing the FT-IR spectrum of Figure 5a for SMR and Figure 5b for DMR, it is clear that panels 1 provide information on the asymmetric stretching vibrations of the C−H bonds. We refer here to Table 2 for an overview of the literature-based FT-IR peak assignments used in this work.[41,49−52] The self-supported wafers of catalyst 6, likely due to its relatively high Ni weight loading, always deform during reduction, which causes resonance IR vibrations to occur in the CO stretching vibration region, hindering us from obtaining useful information from the operando FT-IR spectra. This is as shown in the Supporting Information. Panel 2 in Figures 5a,b show the CO and CO_2 asymmetric stretching vibration region, whereas panel 3 shows the $CO_{(ads)}$ stretching vibration region where different reaction intermediates are expected. Figures 5c,d show panel 3 of Figures 5a,b, the CO_{ads}

Table 2. Overview of the FT-IR Peak Assignments Used in This Work

FT-IR peak (cm^{-1})	assignment
3015	CH asymmetric stretch $CH_{4(g)}$ [41]
3011	CH asymmetric stretch $CH_{4(aq)}$ [49]
2370−2290	$CO_{2(g)}$ asymmetric stretch [50]
2047−2014	$CO_{ads\text{-}top}$ [50,51]
1915−1870	$CO_{ads\text{-}bridge}$ [52]
1630	H_2O_{ads}

DOI: 10.1021/acscatal.9b04193
ACS Catal. 2020, 10, 1428−1438

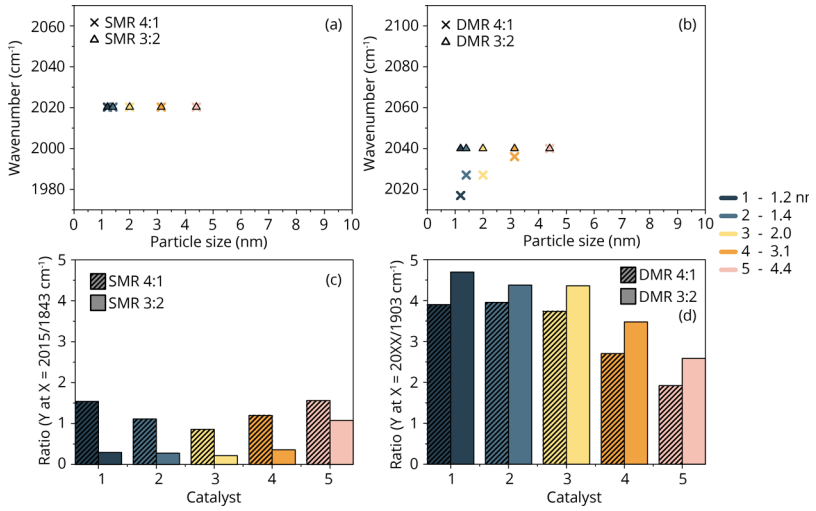

Figure 6. (a) Ratio of the $CO_{ads\text{-}top}$ vs $CO_{ads\text{-}bridge}$ peaks at their respective positions at 2020 and 1843 cm^{-1} for SMR at a feedstock ratio of CH_4/H_2O of 4:1 and 3:2. (b) Ratio of the $CO_{ads\text{-}top}$ vs $CO_{ads\text{-}bridge}$ peaks at their respective positions for DMR at a feedstock ratio of CH_4/CO_2 of 4:1 and 3:2. *X* position of the maximum *Y* value in the wavenumber range 1980−2100 cm^{-1} for (c) SMR and (d) DMR, corresponding to position of the $CO_{ads\text{-}top}$, or for catalyst 6 in DMR 4:1, $CO_{(g)}$.

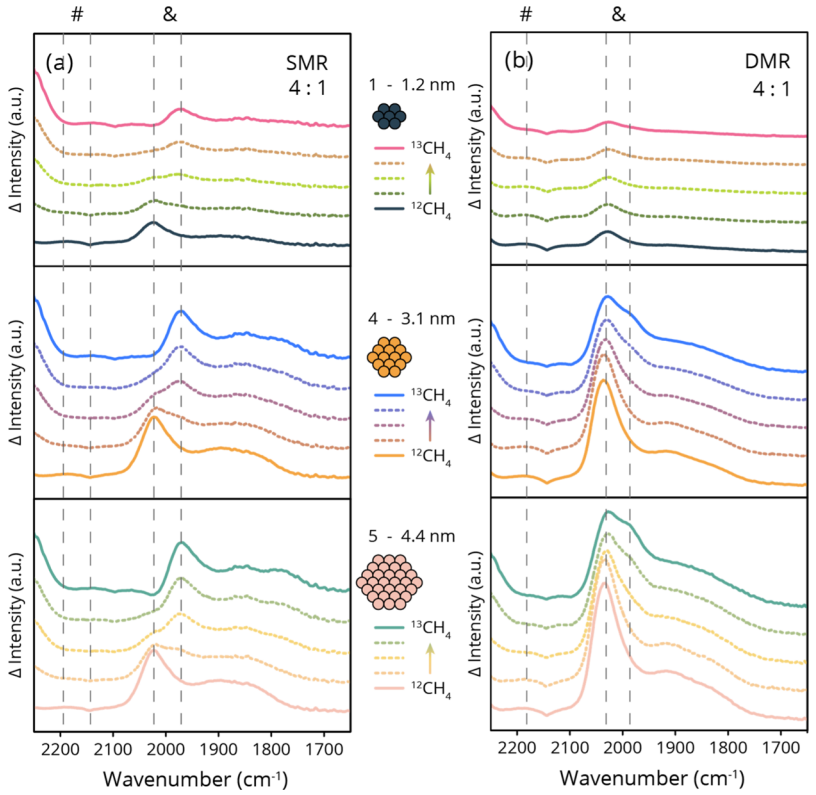

Figure 7. Overview of CO_2 and CO vibration region in FT-IR during a pulsed experiment from $^{12}CH_4$ to $^{13}CH_4$ for both SMR (a) and DMR (b) shown here for 500 °C and 4:1 ratio of CH_4/H_2O at atmospheric pressure. Symbols indicate the area where a shift from $^{12}CO_{(g)}$ to $^{13}CO_{(g)}$ (#) and $^{12}CO_{ads\text{-}top}$ to $^{13}CO_{ads\text{-}top}$ (&) is expected.

stretching vibration region, for SMR and DMR at a reactant ratio of 3:2. Here, two binding modes of CO, a proposed surface reaction intermediate, can be observed with peak maxima between 2047 and 2014 cm^{-1} in top position, and 1915−1870 cm^{-1} in bridge position.[51,53−55]

CO_{ads} strongly influences the rate of the reaction, as found by Rostrup-Nielsen et al., as CO formation and desorption are steps that are both involved in SMR and DMR on the same Ni catalyst.[56] In Figures 6a,b, the maximum peak position of CO in the window 1980−2100 cm^{-1} is plotted. If we compare these CO peak maximum positions in DMR and SMR, a bathochromic peak shift can be observed for SMR. The maximum for the $CO_{ads\text{-}top}$ peak position is located at approximately 2020 cm^{-1}, whereas in DMR, this species can be found roughly around 2040 cm^{-1}. This indicates higher surface coverage of CO_{ads} in the case of DMR, which can be explained by the formation of CO both from CH_4, and CO_2 in DMR, which is also apparent in our yield (Figure S8). The

DOI: 10.1021/acscatal.9b04193
ACS Catal. 2020, 10, 1428−1438

desorption of CO might be kinetically slow relative to other reaction steps for DMR. It is interesting to see that the position of the $CO_{ads\text{-}top}$ peak also changes with respect to Ni metal nanoparticle size for an excess of methane. This confirms that the higher surface coverage of $CO_{ads\text{-}top}$ is caused by the formation of it also from CO_2.

Furthermore, the ratio after 10 min time-on-stream at 500 °C of this $CO_{ads\text{-}top}$ versus bridge position in the difference spectra where the first spectrum is subtracted from each subsequent spectrum is plotted in Figure 6c for SMR and 6d for DMR. For SMR, the relative amount of $CO_{ads\text{-}top}$ species to $CO_{ads\text{-}bridge}$ species sees a minimum for the most active catalyst. This may indicate that $CO_{ads\text{-}top}$ is optimally consumed in a consecutive step in the reaction, or it could mean that $CO_{ads\text{-}bridge}$ is the active species although the latter is unlikely due to its more stable configuration. For the ratio of 3:2 versus 4:1, less methane present gives a lower ratio of $CO_{ads\text{-}top}$ to $CO_{ads\text{-}bridge}$ in SMR, which can be explained by a lower surface coverage of CO_{ads}.

For DMR, the ratio of $CO_{ads\text{-}top}$ versus $CO_{ads\text{-}bridge}$ correlates positively to the observed TOF trend in Figures 2e,f. Yet the overall ratio of CO_{ads} species is much higher because the CO_{ads} is formed also from CO_2 in DMR. Nevertheless, for SMR we see a negative correlation in the ratio of $CO_{ads\text{-}top}$ to $CO_{ads\text{-}bridge}$ whereas for DMR we see positive correlation. Here, we should keep in mind that for CO_{ads} to form in SMR, C and O must recombine, whereas in DMR CO_2 can also form CO_{ads}, and third that the ratio of $CO_{ads\text{-}top}$ to $CO_{ads\text{-}bridge}$ is coverage-dependent. This difference in correlation to activity is telling and it suggests that two different factors kinetically limit each reaction. For DMR, it is likely the recombination of C and O, or the activation of CO_2 is slower than the desorption of CO, whereas for SMR the desorption of CO is what limits under the applied reaction conditions.

Isotopically Labeled Experiments. To gain more insight into the rate-determining step for both SMR and DMR, isotopically labeled experiments were performed with carbon-13-labeled methane and for SMR also with D_2O. By switching between CH_4 and $^{13}CH_4$, or H_2O and D_2O, and acquiring operando FT-IR spectra, we are able to distinguish a difference in reactivity toward the reaction intermediates on the catalyst surface.

Figures 7a,b show SMR and DMR experiments in which the CH_4 feed was switched to $^{13}CH_4$ during the reaction. These data were acquired for 500 °C, and 3:2 and 4:1 feedstock ratio and at 1 bar. After switching to isotopically labeled feedstock, one expects a shift in the IR peak position in the case that (1) the peak contains the same atom as the isotopically labeled switch and (2) the peak is still reactive. For example, upon switching from $^{12}CH_4$ to $^{13}CH_4$, one might expect the $CO_{ads\text{-}top}$ peak to shift if there is still interplay between the feedstock and the species on the surface. For the three different particle sizes shown, 1.2, 3.1, and 4.4 nm, a bathochromic shift of the $CO_{(g)}$ and $CO_{ads\text{-}top}$ signals is observed for all particle sizes because of the formation of $^{13}CO_{(g)}$ (indicated by the dotted line shift #) and $^{13}CO_{ads\text{-}top}$ (indicated by the dotted line shift &). This indicates that the recombination rate of C and O is not strongly structure sensitive for SMR, although it can be kinetically slow. For DMR, however, the smallest catalyst particle size has less of a shift in the $CO_{(g)}$ and $CO_{ads\text{-}top}$ stretching vibration peak, as the shoulder at approximately 1983 cm^{-1} in Figure 7b can hardly be observed. Figure 8a displays the FT-IR spectrum of catalyst 1 and 5 (1.2 and 4.4 nm, Table 1) during DMR using labeled $^{13}CH_4$. It serves to show that there is indeed an absence of a significant shoulder in the $CO_{ads\text{-}top}$ peak for the 1.2 nm nanoparticle. Although it may be expected that there is less of a shift for DMR than SMR, as CO species for DMR may be produced both by the isotopically labeled CH_4, and the non-isotopically labeled CO_2, the difference in particle size within the set of DMR experiments is striking. The absence of a significant shoulder for 1.2 nm particles after switching, with its presence for the larger, 4.4 nm mean Ni particles (indicated by # in Figure 8a), indicates that for the small Ni particles the desorption of $CO_{ads\text{-}top}$ may become more of a kinetically limiting factor.

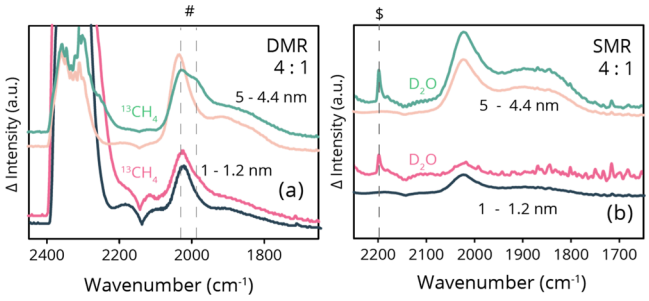

Figure 8. (a) Top and bottom spectra from Figure 7b (1.2 nm, and 4.4 nm Ni/SiO_2), showing the absence of the shoulders at approximately 2100 and 1983 cm^{-1} ($^{13}CO_{ads\text{-}top}$). The (expected) shift is indicated by #. (b) D_2O-fed experiment for SMR, where a peak arises at approximately 2199 cm^{-1} because of CH_3D formation (indicated by $).

CH_4 activation remains an important discussion factor in the classification of structure sensitivity of SMR and DMR, and reaction kinetics of these reactions as a whole. To gain insight into this reaction step, we also performed isotopically labeled experiments with water. Figure 8b shows spectra for catalysts 1 and 5, in which under normal reaction conditions the water feedstock for SMR was switched to D_2O. Upon the introduction of D_2O, for both particle sizes a sharp peak arises at 2199 cm^{-1}. This peak can unambiguously be assigned to CH_3D, which is highly interesting as if one were to assume Langmuir Hinshelwood kinetics, one may assume every catalytic reaction step to be reversible, except for the rate-determining step (or for it to be significantly slower than the forward reaction).[2,3] Keeping this in mind, this indicates that for both 4:1, and 3:2 ratios of $CH_4/H_2O/D_2O$, methane activation is not the (only) rate-limiting step.

Carbon Formation. Not only are the desired gaseous products believed to have structural dependence, but also the formation of carbon deposits is believed to be structure sensitive over supported Ni nanoparticles,[20,57] though no systematic study has as of yet been performed to the best of our knowledge. For both SMR and DMR, carbon formation is known to occur, and it can interfere with the activity of the reaction. To this end, TGA–MS experiments were performed to determine the carbon content of each spent catalyst sample with different mean Ni particle sizes. Figures 9a–d show the percentage of weight loss determined by TGA for each of the analyzed spent samples for SMR and DMR reacted at 500 and 600 °C and the two different feedstock ratios studied (4:1 and 3:2 $CH_4/CO_2/H_2O$). The Supporting Information, section "Carbon formation", gives more details about the TGA profiles and also displays the residual weight fractions with time-on-stream during the TGA measurements, and the MS data for each experiment (Figures S25–28). Furthermore, Figure S29

DOI: 10.1021/acscatal.9b04193
ACS Catal. 2020, 10, 1428–1438

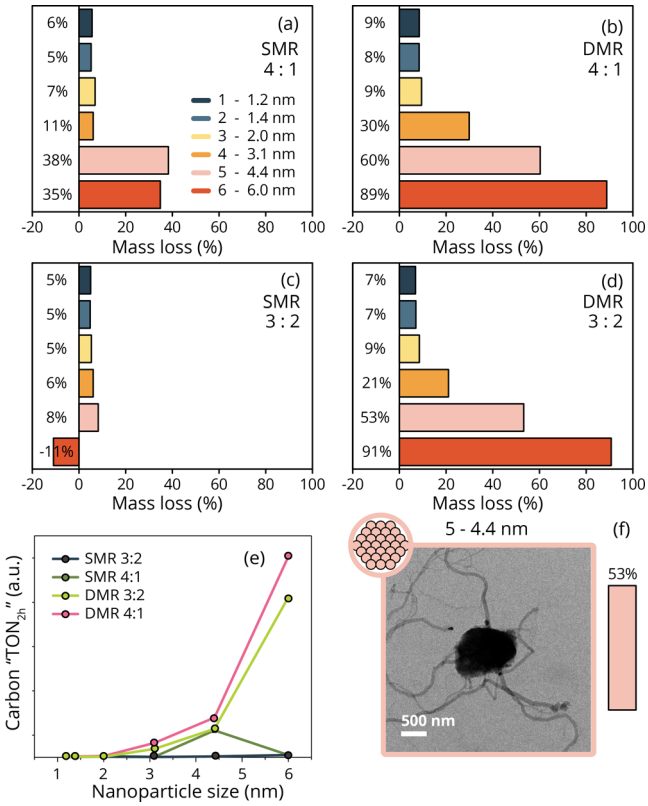

Figure 9. (a–d) TGA of the catalysts after SMR and DMR at 500 and 600 °C, residual weight fraction is shown in % weight loss during TGA. (e) Carbon "TON_{2h}" calculated based on integrated carbon MS profiles during TGA, and the exposed Ni surface area for each catalyst. (f) Representative transmission electron micrograph showing C whiskers, of catalyst 5. The Supporting Information section "Carbon formation" shows micrographs for all spent catalysts.

shows a schematic of the types of carbon whisker formation that can occur.

For a ratio of 3:2 in SMR, the catalyst with the largest mean Ni particle size shows a weight increase during the TGA measurements likely due to the incomplete oxidation of the carbon deposits and/or nickel oxidation during the TGA. Nevertheless, one can note a particle size dependence in the absolute amount of C that was formed for the different catalysts. That is, generally, the larger the mean Ni particle size, the more carbon seems to have formed. This is reflected also in the MS data of the TGA–MS experiments (Figure S28). Nevertheless, keeping in mind that the different catalyst particle sizes have different nominal weight loadings of Ni and hence exposed surface area, it is much more telling to determine the surface-normalized C formation. This is interesting both in terms of stability of the SMR and DMR catalysts during reaction as C formation can deactivate our catalysts, but it is also useful information if one were to want to use CH_4 to produce C materials as discussed in the introduction.[43] It is clear from the carbon TON_{2h} in Figure 9e, that there is also a particle size-dependent trend in the surface-normalized formation of carbon whiskers over Ni. That is, the surface-normalized amount of carbon formation increases with increasing nanoparticle size for DMR. For SMR, this particle size dependence is less significant, and a slight maximum (at a ratio of 3:2) or no significant particle size dependence (at a ratio of 4:1) is observed. Bengaard et al. found that lowering the Ni crystallite size decreases the rate of formation of C, and increases the initial temperature of carbon formation.[58] This is in line with the findings in this work. Figure 9f shows a representative TEM micrograph of the carbon whiskers that occurred for some of the catalysts during reaction. The Supporting Information shows further TEM analysis of the spent samples, and shows clear particle size-dependent carbon whisker formation (Figures S30–S37).

The slightly higher maximum particle size for increased C formation with respect to the most active particle size in terms of CO and H_2 production indicates that for these slightly larger particles the activation of the oxidant (i.e., CO_2 or H_2O) becomes kinetically limiting, or the formation of C occurs faster on the slightly larger particles with more highly coordinated sites. Finally, it is interesting to see in Figures S12 and S14 that deactivation in all gaseous products is more significant for smaller mean Ni particle sizes than larger ones. This may indicate that sintering is a more significant deactivation mechanism in SMR and DMR than the formation of C is, as larger particles form more carbon but are less deactivated. Finally, from these figures, we can see that the production of larger amounts of C for larger particles logically goes hand in hand with an increased production of H_2. In this way, if carbon formation can be managed in the reactor, and the reactors would be operating outside of thermodynamic equilibrium, the ratio of H_2/CO could be tuned through particle size.

CONCLUDING REMARKS

The experiments in this work have shown that very small (<~1.5 nm) supported Ni nanoparticles are less active in both SMR and DMR, and we have explained why. There must be a balance in the sites that optimally activate σ-bonds and those that activate π-bonds; it follows from logic that a combination of different sites is necessary for the reaction to optimally occur. Furthermore, we prove that CH_4 activation is not the (only) rate-limiting step in SMR under the tested reaction conditions by isotopically labeled experiments in Figure 8b. In most catalytic reactions, both σ- and π-bonds will be formed and the rate-determining step will vary with particle size. For small nanoclusters (<~ 2.5 nm), quantum effects may also play a role. Quantum effects can arise for Ni metal nanoparticles below approximately 560 Ni atoms,[29−31] or corresponding to approximately 2.5 nm for Ni nanoparticles. Hence, the inclusion of such small transition-metal nanoparticle sizes as we have done in this study is very important to establish relevant structure sensitivity trends over Ni.

To summarize, by using a set of six catalyst materials consisting of well-defined Ni metal nanoparticles supported on SiO_2 in the range of 1.2–6.0 nm, particle size effects in the activity and the formation of carbon during SMR and DMR were assessed. There is a particle size dependency in the TOF toward desired end products (CO and H_2), a maximum at a particle size of approximately 2–3 nm. Figure S15 displays the TOF trends from literature as also shown in Figure 3, but with the data presented in this work added to it. Furthermore, a Ni particle size dependence in the formation of carbon whiskers was found. A maximum in the surface normalized carbon formation was found at approximately 4 nm for SMR, and an increasing amount of carbon was observed in DMR for larger nanoparticle sizes. This difference in maxima shows that for larger nanoparticles, the activation of the oxidant (CO_2 or H_2O) becomes kinetically limiting. By use of operando

DOI: 10.1021/acscatal.9b04193
ACS Catal. 2020, 10, 1428−1438

spectroscopy, we have found that the predominant pathway for syngas formation is the direct carbide pathway. By the inclusion of also very small SiO_2-supported Ni nanoparticles there is likely not one absolute rate-limiting step. By these methods, we were able to determine that the rate-determining step in this reaction is dependent on the ratio of feedstock applied to the system and that the activation of methane is not the (only) rate-limiting step, as we observe the formation of CH_3D upon pulsing D_2O. The recombination of C and O to form CO, and the desorption thereof are likely also important kinetically limiting factors in SMR and DMR, which we base on isotopically labeled experiments. These combined insights show that the optimal particle size in terms of (short term) stability and activity toward the desired products in both SMR and DMR is approximately 2−3 nm. Furthermore, we propose that the proper manner to portray the TOF trend of SMR and DMR is with decreasing activity for nanoclusters.

■ ASSOCIATED CONTENT

Supporting Information

The Supporting Information is available free of charge at https://pubs.acs.org/doi/10.1021/acscatal.9b04193.

> The Supporting Information is available free of charge on the ACS Publications website. List of various literature data, and additional characterization (TEM), activity (GC), spectroscopy (FT-IR), and data on carbon formation (TGA, TEM) (PDF)

■ AUTHOR INFORMATION

Corresponding Author

*Email: B.M.Weckhuysen@uu.nl.

ORCID

Bert M. Weckhuysen: 0000-0001-5245-1426

Author Contributions

The paper was written through contributions of all the authors. All the authors have given approval to the final version of the paper.

Funding

The authors thank BASF and NWO for a TA-CHIPP grant, and also ARC CBBC for research funding.

Notes

The authors declare no competing financial interest.

■ ACKNOWLEDGMENTS

BASF and NWO are thanked for research funding. ARC CBBC is also thanked for research funding.

■ REFERENCES

(1) Rostrup-Nielsen, J. R.. In *Catalysis: Science and Technology*; Anderson, J. R., Boudart, M., Eds.; Springer-Verlag: Berlin, 1984; pp 1−117.

(2) Dumesic, J. A.; Huber, G. W.; Boudart, M. In *Handbook of Heterogeneous Catalysis*; Ertl, G., Knözinger, H., Schüth, F., Weitkamp, J., Eds.; Wiley-VCH: Weinheim, 2008; pp 1445−1462.

(3) *Handbook of Heterogeneous Catalysis*, 2nd ed; Ertl, G., Knözinger, H., Schüth, F., Weitkamp, J., Eds.; Wiley-VCH: Weinheim, 2008.

(4) Schlögl, R. E-Mobility and the Energy Transition. *Angew. Chem., Int. Ed.* **2017**, *56*, 11019−11022.

(5) Schlögl, R. The Revolution Continues: Energiewende 2.0. *Angew. Chem., Int. Ed.* **2015**, *54*, 4436−4439.

(6) de Smit, E.; Swart, I.; Creemer, J. F.; Hoveling, G. H.; Gilles, M. K.; Tyliszczak, T.; Kooyman, P. J.; Zandbergen, H. W.; Morin, C.; Weckhuysen, B. M.; de Groot, F. M. F. Nanoscale Chemical Imaging of a Working Catalyst by Scanning Transmission X-ray Microscopy. *Nature* **2008**, *456*, 222−225.

(7) Anderson, R. B.; Schultz, J. F.; Hofer, L. J. E.; Storch, H. H. *Bur. Mines Bull.. 580*, **1959**.

(8) Xie, J.; Paalanen, P. P.; van Deelen, T. W.; Weckhuysen, B. M.; Louwerse, M. J.; de Jong, K. P. Promoted Cobalt Metal Catalysts Suitable for the Production of Lower Olefins from Natural Gas. *Nat. Commun.* **2019**, *10*, 167.

(9) Mette, K.; Kühl, S.; Tarasov, A.; Düdder, H.; Kähler, K.; Muhler, M.; Schlögl, R.; Behrens, M. Redox dynamics of Ni catalysts in CO_2 reforming of methane. *Catal. Today* **2015**, *242*, 101−110.

(10) Vogt, C.; Monai, M.; Kramer, G. J.; Weckhuysen, B. M. The Renaissance of the Sabatier Reaction and its Applications on Earth and in Space. *Nat. Catal.* **2019**, *2*, 188−197.

(11) Gao, J.; Hou, Z.; Lou, H.; Zheng, X. In *Fuel Cells: Technologies for Fuel Processing*; Shekhawat, D., Spivey, J. J., Berry, D., Eds.; Elsevier: Amsterdam, 2011; pp 191−221.

(12) Wang, H. Y.; Ruckenstein, E. Partial Oxidation of Methane to Synthesis Gas over Alkaline Earth Metal Oxide Supported Cobalt Catalysts. *J. Catal.* **2001**, *199*, 309−317.

(13) Centi, G.; Perathoner, S. Opportunities and prospects in the chemical recycling of carbon dioxide to fuels. *Catal. Today* **2009**, *148*, 191−205.

(14) Wang, F.; Li, W.-Z.; Lin, J.-D.; Chen, Z.-Q.; Wang, Y. Crucial support effect on the durability of $Pt/MgAl_2O_4$ for partial oxidation of methane to syngas. *Appl. Catal. B Environ.* **2018**, *231*, 292−298.

(15) Liu, R.-S.; Iwamoto, M.; Lunsford, J. H. Partial Oxidation of Methane by Nitrous Oxide over Molybdenum Oxide Supported on Silica. *J. Chem. Soc., Chem. Commun.* **1982**, *1*, 78−79.

(16) Vermeiren, W. J. M.; Blomsma, E.; Jacobs, P. A. Catalytic and Thermodynamic Approach of the Oxyreforming Reaction of Methane. *Catal. Today* **1992**, *13*, 427−436.

(17) van Looij, F.; van Giezen, J. C.; Stobbe, E. R.; Geus, J. W. Mechanism of the Partial Oxidation of Methane to Synthesis Gas on a Silica-Supported Nickel Catalyst. *Catal. Today* **1994**, *21*, 495−503.

(18) Erdöhelyi, A.; Cserényi, J.; Papp, E.; Solymosi, F. Catalytic reaction of methane with carbon dioxide over supported palladium. *Appl. Catal. Gen.* **1994**, *108*, 205−219.

(19) Guo, X.; Sun, Y.; Yu, Y.; Zhu, X.; Liu, C.-j. Carbon Formation and Steam Reforming of Methane on Silica Supported Nickel Catalysts. *Catal. Commun.* **2012**, *19*, 61−65.

(20) Christensen, K. O.; Chen, D.; Lødeng, R.; Holmen, A. Effect of Supports and Ni Crystal Size on Carbon Formation and Sintering During Steam Methane Reforming. *Appl. Catal. Gen.* **2006**, *314*, 9−22.

(21) Lin, C.; Jang, J. B.; Zhang, L.; Stach, E. A.; Gorte, R. J. Improved Coking Resistance of "Intelligent" Ni Catalysts Prepared by Atomic Layer Deposition. *ACS Catal.* **2018**, *8*, 7679−7687.

(22) Yamazaki, O.; Tomishige, K.; Fujimoto, K. Development of highly stable nickel catalyst for methane-steam reaction under low steam to carbon ratio. *Appl. Catal. Gen.* **1996**, *136*, 49−56.

(23) Urasaki, K.; Kado, S.; Kiryu, A.; Imagawa, K.-i.; Tomishige, K.; Horn, R.; Korup, O.; Suehiro, Y. Synthesis Gas Production by Catalytic Partial Oxidation of Natural Gas Using Ceramic Foam Catalyst. *Catal. Today* **2018**, *299*, 219−228.

(24) Bennett, C. O.; Che, M. Some Geometric Aspects of Structure Sensitivity. *J. Catal.* **1989**, *120*, 293−302.

(25) Che, M.; Bennett, C. O. The Influence of Particle Size on the Catalytic Properties of Supported Metals. *Adv. Catal.* **1989**, *36*, 55−172.

(26) van Santen, R. A. Complementary Structure Sensitive and Insensitive Catalytic Relationships. *Acc. Chem. Res.* **2009**, *42*, 57−66.

(27) van Hardeveld, R.; van Montfoort, A. The influence of crystallite size on the adsorption of molecular nitrogen on nickel, palladium and platinum. *Surf. Sci.* **1966**, *4*, 396−430.

(28) Somorjai, G. A.; Contreras, A. M.; Montano, M.; Rioux, R. M. Clusters, Surfaces, and Catalysis. *Proc. Natl. Acad. Sci. U.S.A.* **2006**, *103*, 10577−10583.

DOI: 10.1021/acscatal.9b04193
ACS Catal. 2020, 10, 1428−1438

(29) Melaet, G.; Lindeman, A. E.; Somorjai, G. A. Cobalt Particle Size Effects in the Fischer-Tropsch Synthesis and in the Hydrogenation of CO_2 Studied with Nanoparticle Model Catalysts on Silica. *Top. Catal.* **2014**, *57*, 500−507.
(30) Hibbitts, D.; Dybeck, E.; Lawlor, T.; Neurock, M.; Iglesia, E. Preferential Activation of CO Near Hydrocarbon Chains During Fischer-Tropsch Synthesis on Ru. *J. Catal.* **2016**, *337*, 91−101.
(31) van den Berg, R.; Prieto, G.; Korpershoek, G.; van der Wal, L. I.; van Bunningen, A. J.; Lægsgaard-Jørgensen, S.; de Jongh, P. E.; de Jong, K. P. Structure Sensitivity of Cu and CuZn Catalysts Relevant to Industrial Methanol Synthesis. *Nat. Commun.* **2016**, *7*, 13057.
(32) Wei, J.; Iglesia, E. Structural Requirements and Reaction Pathways in Methane Activation and Chemical Conversion Catalyzed by Rhodium. *J. Catal.* **2004**, *225*, 116−127.
(33) Wang, Y.; Wang, H.; Dam, A. H.; Xiao, L.; Qi, Y.; Niu, J.; Yang, J.; Zhu, Y.-A.; Holmen, A.; Chen, D. Understanding Effects of Ni Particle Size on Steam Methane Reforming Activity by Combined Experimental and Theoretical Analysis. *Catal. Today* **2019**, DOI: 10.1016/j.cattod.2019.04.040.
(34) Xu, J.; Froment, G. F. Methane steam reforming, methanation and water-gas shift: I. Intrinsic kinetics. *AIChE J.* **1989**, *35*, 88−96.
(35) Kageyama, N.; Devocht, B. R.; Takagaki, A.; Toch, K.; Thybaut, J. W.; Marin, G. B.; Oyama, S. T. Interplay of Kinetics and Thermodynamics in Catalytic Steam Methane Reforming over Ni/MgO-SiO2. *Ind. Eng. Chem. Res.* **2017**, *56*, 1148−1158.
(36) Hou, K.; Hughes, R. The kinetics of methane steam reforming over a Ni/α-Al_2O catalyst. *Chem. Eng. J.* **2001**, *82*, 311−328.
(37) Bezemer, G. L.; Bitter, J. H.; Kuipers, H. P. C. E.; Oosterbeek, H.; Holewijn, J. E.; Xu, X.; Kapteijn, F.; van Dillen, A. J.; de Jong, K. P. Cobalt Particle Size Effects in the Fischer−Tropsch Reaction Studied with Carbon Nanofiber Supported Catalysts. *J. Am. Chem. Soc.* **2006**, *128*, 3956−3964.
(38) Boudart, M. Catalysis by Supported Metals. *Adv. Catal.* **1969**, *20*, 153−166.
(39) Rostrup-Nielsen, J. R. Activity of Nickel Catalysts for Steam Reforming of Hydrocarbons. *J. Catal.* **1973**, *31*, 173−199.
(40) Sárkány, A.; Tétényi, P. On the structure sensitivity of ethane hydrogenolysis on Ni catalysts. *React. Kinet. Catal. Lett.* **1979**, *12*, 297−301.
(41) Vogt, C.; Groeneveld, E.; Kamsma, G.; Nachtegaal, M.; Lu, L.; Kiely, C. J.; Berben, P. H.; Meirer, F.; Weckhuysen, B. M. Unravelling structure sensitivity in CO_2 hydrogenation over nickel. *Nat. Catal.* **2018**, *1*, 127−134.
(42) van Helden, P.; Ciobîcă, I. M.; Coetzer, R. L. J. The size-dependent site composition of FCC cobalt nanocrystals. *Catal. Today* **2016**, *261*, 48−59.
(43) Upham, D. C.; Agarwal, V.; Khechfe, A.; Snodgrass, Z. R.; Gordon, M. J.; Metiu, H.; McFarland, E. W. Catalytic Molten Metals for the Direct Conversion of Methane to Hydrogen and Separable Carbon. *Science* **2017**, *358*, 917−921.
(44) Ermakova, M. A.; Ermakov, D. Y. High-loaded nickel-silica catalysts for hydrogenation, prepared by sol-gel. *Appl. Catal. Gen.* **2003**, *245*, 277−288.
(45) Trimm, D. L. Catalysts for the Control of Coking During Steam Reforming. *Catal. Today* **1999**, *49*, 3−10.
(46) Hassan, H.; Khandelwal, B. Reforming Technologies to Improve the Performance of Combustion Systems. *Aerospace* **2014**, *1*, 67−96.
(47) Mundhwa, M.; Thurgood, C. P. Methane steam reforming at low steam to carbon ratios over alumina and yttria-stabilized-zirconia supported nickel-spinel catalyst: Experimental study and optimization of microkinetic model. *Fuel Process. Technol.* **2017**, *168*, 27−39.
(48) Guo, J.; Lou, H.; Zhao, H.; Chai, D.; Zheng, X. Dry Reforming of Methane over Nickel Catalysts Supported on Magnesium Aluminate Spinels. *Appl. Catal. Gen.* **2004**, *273*, 75−82.
(49) Schädle, T.; Pejcic, B.; Mizaikoff, B. Monitoring Dissolved Carbon Dioxide and Methane in Brine Environments at High Pressure using IR-ATR Spectroscopy. *Anal. Methods* **2016**, *8*, 756−762.
(50) Weststrate, C. J.; van de Loosdrecht, J.; Niemantsverdriet, J. W. Spectroscopic Insights into Cobalt-Catalyzed Fischer-Tropsch Synthesis: A Review of the Carbon Monoxide Interaction with Single Crystalline Surfaces of Cobalt. *J. Catal.* **2016**, *342*, 1−16.
(51) Courtois, M.; Teichner, S. J. Infrared studies of CO, O_2, and CO_2 gases and their interaction products, chemically adsorbed on nickel oxide. *J. Catal.* **1962**, *1*, 121−135.
(52) Madden, H. H. of Carbon Monoxide with (110) Nickel Surfaces. *J. Chem. Phys.* **1973**, *58*, 3401.
(53) Campuzano, J. C.; Greenler, R. G. The Adsorption Sites of CO on Ni(111) as Determined by Infrared Reflection-Absorption Spectroscopy. *Surf. Sci.* **1979**, *83*, 301−312.
(54) Mohsin, S. B.; Trenary, M.; Robota, H. J. Infrared identification of the low-temperature forms of ethylene adsorbed on platinum/alumina. *J. Phys. Chem.* **1988**, *92*, 5229−5233.
(55) Layman, K. A.; Bussell, M. E. Infrared Spectroscopic Investigation of CO Adsorption on Silica-Supported Nickel Phosphide Catalysts. *J. Phys. Chem. B* **2004**, *108*, 10930−10941.
(56) Rostrup-Nielsen, J. R.; Hansen, J. H. B. CO_2-Reforming of Methane over Transition Metals. *J. Catal.* **1993**, *144*, 38−49.
(57) Argyle, M.; Bartholomew, C. Heterogeneous Catalyst Deactivation and Regeneration: A Review. *Catalysts* **2015**, *5*, 145−269.
(58) Bengaard, H. S.; Nørskov, J. K.; Sehested, J.; Clausen, B. S.; Nielsen, L. P.; Molenbroek, A. M.; Rostrup-Nielsen, J. R. Steam Reforming and Graphite Formation on Ni Catalysts. *J. Catal.* **2002**, *209*, 365−384.

DOI: 10.1021/acscatal.9b04193
ACS Catal. 2020, 10, 1428−1438